Experimental Testing and Full and Homogenized Numerical Models of the Low Velocity and Dynamic Deformation of the Trapezoidal Aluminium Corrugated Core Sandwich

C. Kılıçaslan, İ. K. Odacı, A. Taşdemirci and M. Güden

Dynamic Testing and Modeling Laboratory, Department of Mechanical Engineering, Izmir Institute of Technology, Gülbahçe Köyü, Urla, Izmir, Turkey

ABSTRACT: The simulations of the low velocity and dynamic deformation of a multi-layer 1050-H14 Al trapezoidal zig-zag corrugated core sandwich were investigated using the homogenized models (solid models) of a single core layer (without face sheets). In the first part of the study, the LS-DYNA MAT-26 material model parameters of a single core layer were developed through experimental and numerical compression tests on the single core layer. In the second part, the fidelities of the developed numerical models were checked by the split-Hopkinson pressure bar direct impact, low velocity compression and indentation and projectile impact tests. The results indicated that the element size had a significant effect on the initial peak and post-peak stresses of the homogenized models of the direct impact testing of the single-layer corrugated sandwich. This was attributed to the lack of the inertial effects in the homogenized models, which resulted in reduced initial peak stresses as compared with the full model and experiment. However, the homogenized models based on the experimental stress–strain curve of the single core layer predicted the low velocity compression and indentation and projectile impact tests of the multi-layer corrugated sandwich with an acceptable accuracy and reduced the computational time of the models significantly.

KEY WORDS: *corrugated, high strain rate, homogenization, sandwich, simulation*

Introduction

The so-called metallic cellular structures refer to the groups of light-weight metallic materials of various topologies, including honeycombs, foams, lattices and corrugation [1]. These structures are widely used in the applications involving high strain rate loading such as blast and crash. Among these, the corrugated metallic structures have taken considerable interests in recent years as they are easily manufactured into intricate geometries through versatile and conventional sheet metal foaming processes. The corrugated metallic structures have relatively high energy absorption capabilities with directional mechanical properties. These properties are often combined with the multi-functionalities such as good heat exchange and sound absorption [2, 3]. Examples include Y-frame [4, 5], V-frame [4], U-frame [6] and X-frame [7] corrugated core sandwiches in which a single core or multi-layer corrugated cores with and without interlayer sheets is sandwiched between metallic and fibre composite face sheets.

The implementation of the full deformation models of the corrugated core sandwiches is challenging for several reasons. The core models eliminate the arbitrary selection of the element size that directly affects the accuracy of models [8]. The generated mesh size and mesh distribution can also affect the failure significantly [9]. Finally, the numerical core models oblige the use of intricate contact definitions between the individual cores as well as the core and face/interlayer sheets. All these increase the computational time of simulations significantly. The homogenized models

are widely applied in order to shorten the computational time of the deformation models of the metallic cellular structures. The existent literature of the homogenized models is mostly on aluminium honeycomb and foam core sandwiches, and the most widely used codes include MAT-126 [9], MAT-63 [10, 11] and MAT-26 [12, 13] in LS-DYNA, simplified orthotropic material model [14] and shell and macro-solid models in PAM-CRASH [15].

In the present study, the homogenized solid models of the single layer (without face sheets) of 1050-H14 Al trapezoidal zig-zag corrugated core were investigated for simulating the low velocity and dynamic deformation of a multi-layer trapezoidal aluminium corrugated core sandwich in LS-DYNA. The zig-zag form is needed for the transfer of the coolant to the corrugated layer. The tested corrugated layer sandwich forms a closed-loop system for a coolant to circulate within each layer. One of the potential applications with its current form is in the constructions of the ammunition store walls. In this application, the corrugated sandwich walls function in three ways upon an explosion. First, it absorbs the blast through the deformation of the corrugated layers. Second, it provides impact protection against debris by the interlayer sheets. And lastly, the structure supplies coolant to extinguish any fire. Two approaches were adopted in the present study. In the first approach, the MAT-26 material model parameters of the single core layer were determined from the quasi-static compression tests on the single core layer specimen along three different axes. In the second approach, the model parameters were determined from the numerical full model compression testing of the single core layer along the same

three different axes. The fidelities of the developed numerical models were further checked by comparing the results of the homogenized with those of the full model and experimental split-Hopkinson pressure bar (SHPB) direct impact testing of the single-layer corrugated core sandwich and low velocity compression and indentation and projectile impact testing of the multi-layer corrugated core sandwich. It was shown that the material model based on the experimental compression testing of the single core layer yielded nearer results with the full model and experiments. The presented approach reduced the computational time of the dynamic deformation simulation of the multi-layer corrugated core sandwich significantly.

Sandwich Structure Construction

The single- and multi-layer corrugated core sandwiches were constructed using single 1050-H14 Al trapezoidal zig-zag corrugated core (fin) layers as shown in Figure 1A and 1050-H14 Al interlayer sheets and face sheets. The height, width and thickness of the fins of the as-received corrugated core layer are respectively 9, 5 and 0.135 mm (Figure 1B). The thicknesses of the interlayer and face sheets are 0.5 and 1.5 mm, respectively. The sandwiches were assembled through bonding the individual core layers and interlayer and face sheets by applying a thin layer of Thomsit R710 (Henkel, Vienna) polyurethane adhesive. The assemblies were kept under a weight of 10 kg for 2 h after applying the

Figure 1: (A) The picture of a single core layer and (B) fin geometry

adhesive. The square-cross-section quasi-static and SHPB direct impact test single-layer corrugated core specimens (Figure 2A) were 25 mm in length and 12 mm in height. The square-cross-section drop weight compression and indentation and projectile impact test multi-layer corrugated core sandwich specimens were constructed using seven corrugated fin layers, six interlayer sheets and two face sheets. The drop weight compression and indentation and projectile impact test multi-layer corrugated core sandwich specimens were respectively 50 (Figure 2B), 100 (Figure 2C) and 200 mm (Figure 2D) in length and all were 70 mm in height. The density of corrugated fin layer was 115 kg m^{-3}, corresponding to a relative density of 0.042. The density of polyurethane bonded multi-layer corrugated core sandwich was ~370 kg m^{-3}. The details of the test specimen preparation method are given in a previous study [8].

Experiments

The quasi-static compression tests on the single core layer (50 × 50 × 9 mm) and single-layer corrugated core sandwich (25 × 12 mm) were conducted at the strain rate of 10^{-1} s^{-1} in a Shimadzu universal testing machine. The SHPB direct impact testing of the single-layer sandwich was performed in a modified compression SHPB set-up [4]. The used modified SHPB test apparatus consisted of 40-mm diameter 7075-T6 Al bars with the incident bar length of 1000 mm and the striker bar length of 300 mm. The test specimen (25 mm in length and 12 mm in height) was inserted to the front face of the incident bar using a double-sided tape, and the striker bar was fired onto the specimen with a velocity of 18 m s^{-1}. The front stress of the impacted specimen (σ_s) was calculated using the following relation:

$$\sigma_s(t) = \frac{E_b \, A_b}{A_s} \, \varepsilon_i(t) \tag{1}$$

where E_b is the bar modulus (70 GPa), A_b and A_s are sequentially the bar and specimen area, t is the time, and ε_i is the strain on the incident bar measured by the full bridge of 350 Ω strain gages. The specimen front stress was drawn as function of the dimensionless constant of $\frac{v_o t}{H}$, where H is the specimen height and v_o is the striker bar velocity.

The low velocity constraint compression and indentation tests of the multi-layer sandwich were conducted using a Fractovis drop weight tower. The constraint low velocity compression tests were performed by inserting the multi-layer sandwich test specimens in a rectangular closed die (steel), and a cylindrical flat-end 70-mm diameter striker was used to compress the specimen in the closed die at a velocity of 3 m s^{-1}, corresponding to a strain rate of 40 s^{-1}. In order to reduce the friction between the die and specimen, the die walls were lubricated with grease. In the low velocity indentation test, a strain gaged spherical-end
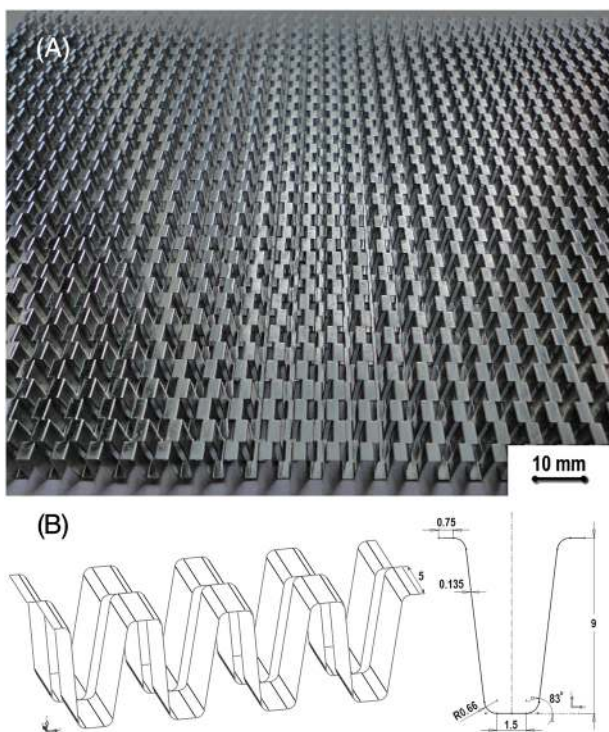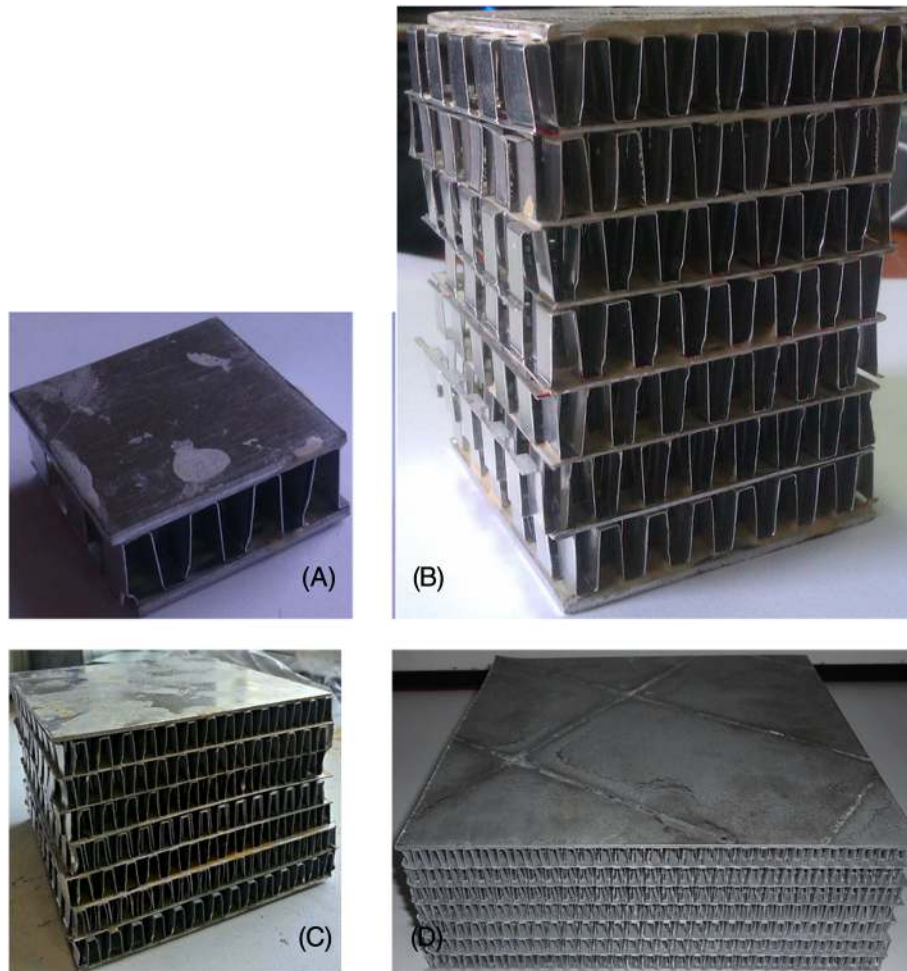
Figure 2: The pictures of (A) single-layer sandwich specimen (25 × 25 × 12 mm) and multi-layer sandwich pecimens having the dimensions of (B) 50 × 50 × 70 mm, (C)100 × 100 × 70 mm and (D) 200 × 200 × 70 mm

striker of 20 mm in diameter indented the test specimen at a velocity of 6 m s^{-1} [8]. The projectile impact tests were performed using a gas-gun projectile impact test set-up. The details of the gas-gun projectile impact test set-up are given in [16]. In these tests, a hardened 30-mm diameter spherical steel projectile was fired against a multi-layer corrugated sandwich target, which was screwed to the target steel frame inside an impact chamber. The initial and residual velocities of the projectile were measured using the laser barriers placed at the front and back of the target frame.

Numerical Modelling

Material models

The numerical models were implemented using the non-linear explicit finite element code LS-DYNA. In the full model, the flow stress of 1050-H14 Al alloy, including corrugated core and interlayer and face sheets, was modelled

using MAT-98 simplified Johnson–Cook material model, which is given as follows [17]:

$$\sigma = [A + B \, \varepsilon^n] \left[1 + c \, ln\left(\frac{\dot{\varepsilon}}{\dot{\varepsilon_0}}\right) \right] \tag{2}$$

where σ, ε, $\dot{\varepsilon}$ and $\dot{\varepsilon_0}$ are the effective stress and effective plastic strain, strain rate and reference strain rate, respectively; A, B, n and c are the model parameters. As the aluminium alloys have no or insignificant strain-rate-dependent flow stress until about ~1000 s^{-1}, the second bracket of Equation [2] was omitted. The Johnson–Cook model parameters and failure strain of the used 1050-H14 Al alloy were previously determined and given as $A = 102$ MPa, $B = 97$ MPa, $n = 0.18$ and the failure strain = 0.62 [8].

In the homogenized models, the deformation of the single fin layer was modelled using MAT-26 honeycomb model in LS-DYNA. The material model MAT-26 is used to represent the elastic–plastic anisotropic behaviour of the cellular materials such as honeycomb and foam [17]. In this

model, the normal compression and shear stress–strain curves along the three axes must be defined separately, and the normal and shear stresses are fully uncoupled in all directions [18]. The strain is

$$\varepsilon = 1 - V \qquad (3)$$

where V is the relative volume: $V = \left(\frac{v}{v_f}\right)$, where v and v_f are the uncompacted and fully compacted element volume, respectively. Elastic modulus (E_{ii}) and shear modulus (G_{ij}) in the uncompacted state are

$$E_{ii} = E_{ii}^{un} + \beta\left(E^{com} - E_{ii}^{un}\right) \qquad (4)$$

and

$$G_{ij} = G_{ij}^{un} + \beta\left(\frac{E^{com}}{2(1+\mu)} - G_{ij}^{un}\right) \qquad (5)$$

respectively. Superscripts *un* and *com* represent sequentially uncompacted and compacted states, μ is the Poisson's ratio and β is given as

$$\beta = \max\left[\min\left(\frac{1-v}{1-v_f}, 1\right), 0\right] \qquad (6)$$

The normal stress (σ_{ii}) and shear stress (σ_{ij}) are then calculated using the following relations:

$$\sigma_{ii}^{n+1} = \sigma_{ii}^{n} + E_{ii}\Delta\varepsilon_{ii} \qquad (7)$$

and

$$\sigma_{ij}^{n+1} = \sigma_{ij}^{n} + 2G_{ij}\Delta\varepsilon_{ij} \qquad (8)$$

where $\Delta\varepsilon_{ii}$ and $\Delta\varepsilon_{ij}$ are the strain increments and n is the time increment.

Numerical models of corrugated core

In the full model, the single-layer corrugated core was meshed with quad Belytschko–Tsay shell elements with five integration points, and interlayer/face sheets were meshed using 1.5×0.75 mm size quad-constant solid elements (Figure 3A–B). The self-contacting interfaces of core layers and interlayer/face sheets were defined by eroding single-layer surface contact type. The contacting surfaces between core layers, interlayer and face sheets were assumed to be perfectly bonded and defined by tied nodes. In the homogenized models, the fin layers in single- and multi-layer sandwiches were meshed with quad-constant solid
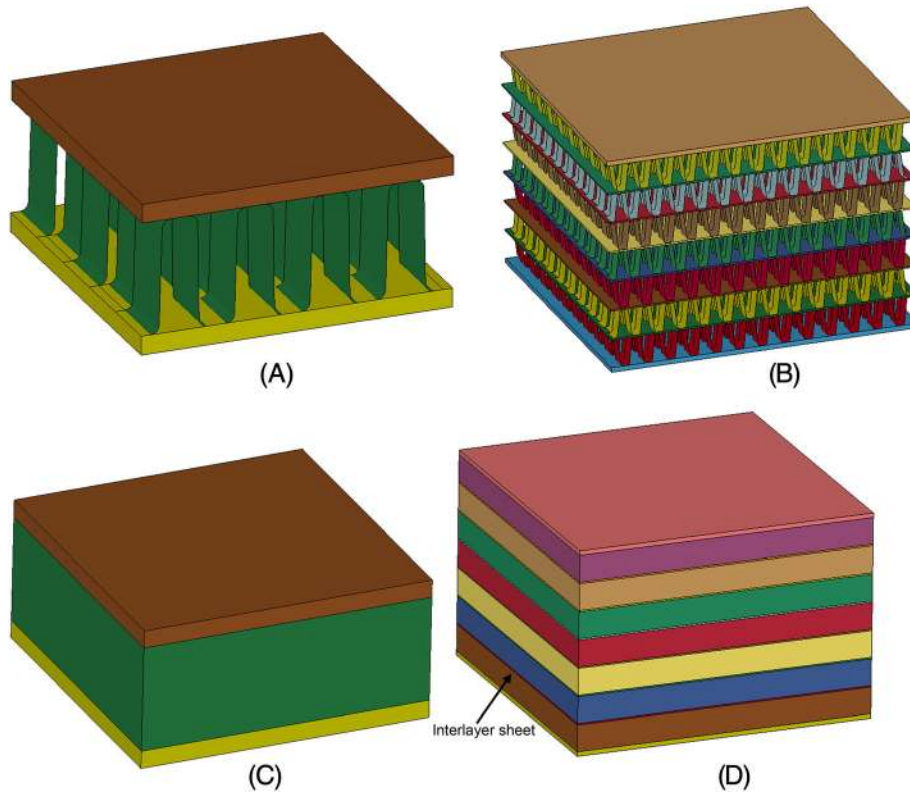

Figure 3: 3D finite element full model of (A) single- and (B)multi-layer sandwich specimen and solid models of (C) single- and (D) multi-layer sandwich specimen

elements (Figure 3C–D). The boding between cores, interlayers and face sheets was assumed to be perfect, and the touching nodes on the contact surfaces were merged using dup-node function in LS-DYNA.

Numerical models of experiments

Figure 4A–C shows the finite element model of the quasi-static compression of the single core layer along the three loading axes of *x*-aa, *y*-bb and *z*-cc, respectively. The quasi-static compression test models consisted of top and bottom platens and a square single core layer. The corrugated core layer was 50 mm in length and width and 9 mm in thickness. The single layer core model is composed of 9800 shell elements. The compression test platens were assumed rigid, and each consisted of 19 200 constant solid elements. The top compression platen moved with a speed of $0.9 \, \mathrm{m \, s^{-1}}$ corresponding to a strain rate of $10^{-1} \, \mathrm{s^{-1}}$, and the bottom platen was kept stationary. The contact between platens and fin layer was defined by the automatic surface to surface contact algorithm. The static and dynamic friction coefficients were taken as 0.3 and 0.2, respectively. The mass scaling was applied by defining a positive constant time step value, as the time steps in the explicit simulations of the quasi-static deformation are relatively small. The stress–strain curves of the simulations were used to construct MAT-26 material model parameters of corrugated layer.

The finite element model of direct SHPB test set-up is shown in Figure 5. The model consisted of the striker and incident bars and the single-layer sandwich specimen. The bars were modelled with MAT-01 elastic material model ($E = 71.7 \, \mathrm{GPa}$ and $v = 0.33$). The striker and incident bar are composed of 23 660 and 33 800 constant stress solid elements, respectively. The single-layer sandwich specimen was meshed with 320 constant solid elements (3 mm in size), called coarse mesh homogenized model, and 2312 constant solid elements (1.5 mm in size), called fine mesh homogenized model. The contact between the bars and specimen was defined by the automatic surface to surface contact algorithm. The striker bar was impacted to the specimen at a velocity of $18 \, \mathrm{m \, s^{-1}}$, the same as the experiments. The stress on the incident bar in the model was determined at an element that had the same distance to the specimen as the strain gages on the incident bar.
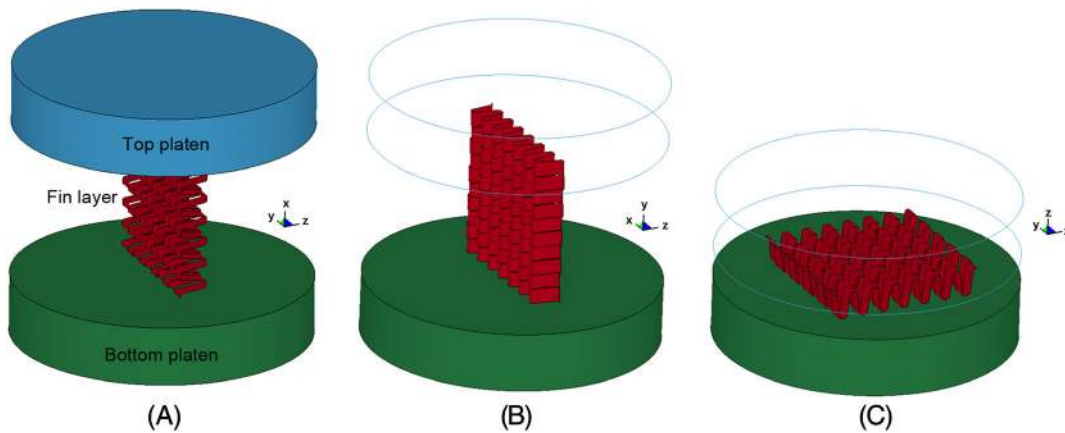

Figure 4: The numerical model of the quasi-static compression of the single core layer along (A) *x*-aa axis, (B) *y*-bb axis and (C) *z*-cc axis
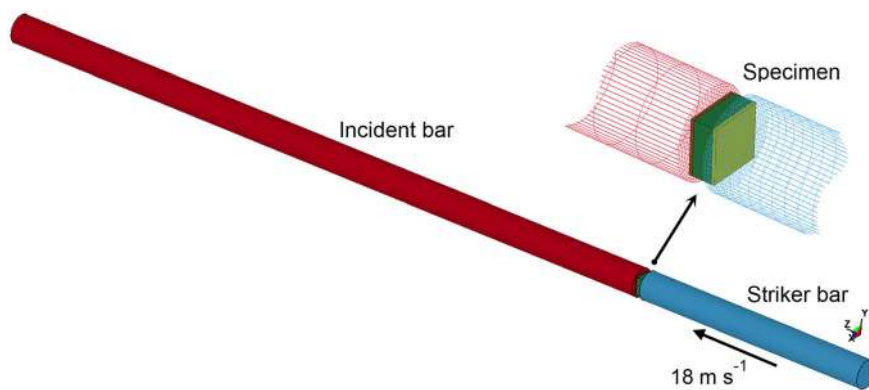

Figure 5: The numerical model of the SHPB direct impact test

Figure 6A and B shows the finite element model of drop weight compression and indentation test, respectively. The compression test model consisted of a flat-end striker, bottom platen and specimen (Figure 6A). The striker and platen were assumed rigid and composed of 106 192 and 5000 constant solid elements, respectively. The compression test specimen was modelled using 119 573 constant solid elements and only allowed to extend in the z-axis
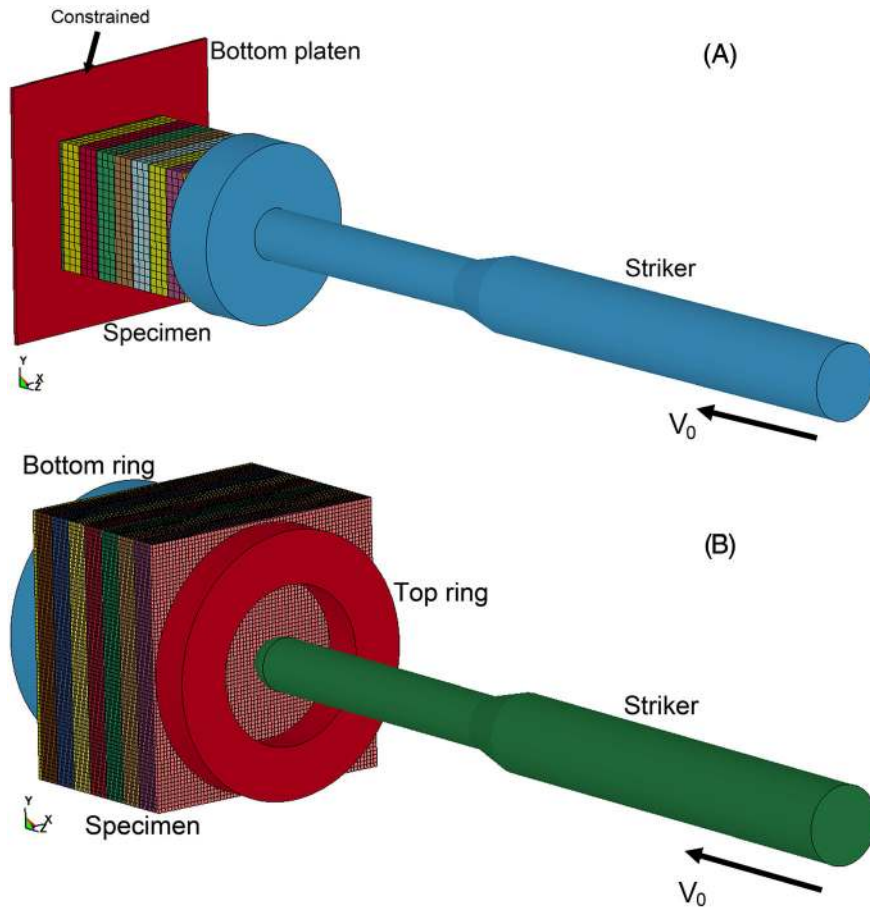

Figure 6: The numerical models of the drop weight (A) compression and (B) indentation test
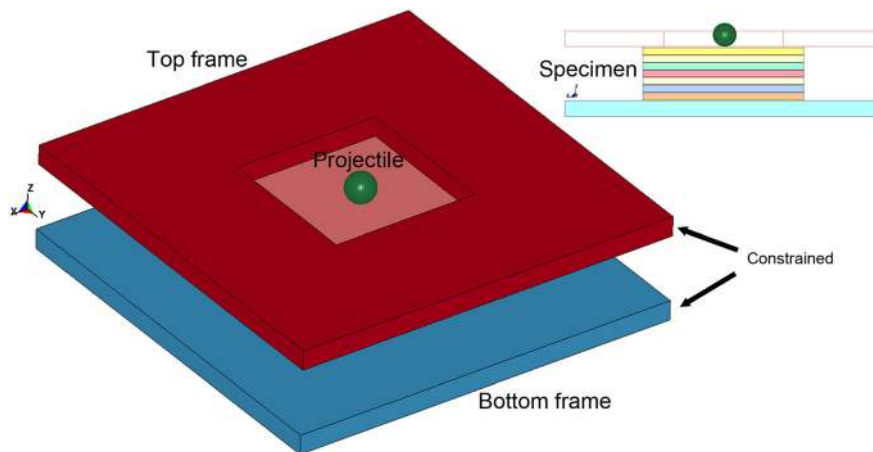

Figure 7: The numerical model of the projectile impact test

(constraint test). The indentation test model consisted of spherical-end striker, rings and specimen (Figure 6B). The striker and rings were assumed rigid and modelled using 73 304 and 5400 constant solid elements, respectively. The indentation test specimen was meshed using 318 719 constant solid elements. The contact between specimen and striker was defined by eroding surface to surface algorithm. The dynamic and static friction coefficients were selected as 0.3 and 0.2 for both contact type.

Figure 7 shows the finite element model of projectile impact test set-up. In the model, the specimen frames, front and back, were taken rigid and modelled using 11 232 solid elements. The projectile was also modelled rigid ($E = 210$ GPa) with an impact velocity of 150 m s^{-1}. The target sandwich specimen was modelled deliberately using the coarse mesh in order to simulate the deformation of large corrugated sandwich plates against projectile impact and included 132 124 constant solid elements. In the actual test, the sandwich specimen in between the frames was tightly fixed through screwing using bolts. The generated compression force due to screwing, ~500 N, was attained in the model to the top frame by defining the model load segment set card in LS-DYNA.

Results and Discussions

Figure 8A–C shows the test and simulation compression stress–strain curves of the single core layer tested in the *x*-, *y*- and *z*-axis at the strain rate of 10^{-1} s^{-1}, respectively. The corresponding simulation undeformed and deformed ($\varepsilon=0.2$ and 0.4) and experimental deformed ($\varepsilon=0.2$ and 0.4) test specimen pictures of the single core layer tested in the *x*-, *y*- and *z*-axis are shown in Figure 9A–C, respectively. The single core layer tested in the *x*-axis deforms elastically under relatively low stresses until about 0.6 strains (Figure 8A). The deformation proceeds with the compression of horizontal fin walls as similar with the elastic compression of an accordion. Above 0.6 strains, the fin wall flat sections however bend both experimentally and numerically over each other under almost a constant stress, 0.2–0.3 MPa (Figures 8A and 9A). At the strains above 0.95, the bent fin walls overlap each other, resulting in an abrupt increase in stress values. The full model simulation stresses are however slightly higher than the experimental stresses as depicted in Figure 8A. The single core layer tested in the *y*- and *z*-axis deform both numerically and experimentally through fin wall buckling (Figure 9B and C), exhibiting type II structure deformation behaviour, a classification made by Calladine and English for the inertia sensitive structures [19]. In type II structure, following the initial peak force, the crushing forces decline gradually as the displacement increases. This is also valid for the single core layer specimen tested in the *y*- and *z*-axis (Figure 8B and C). The simulation and experimental initial peak stresses in the *y*- and *z*-axis are 0.84 and 0.7 MPa and 0.94
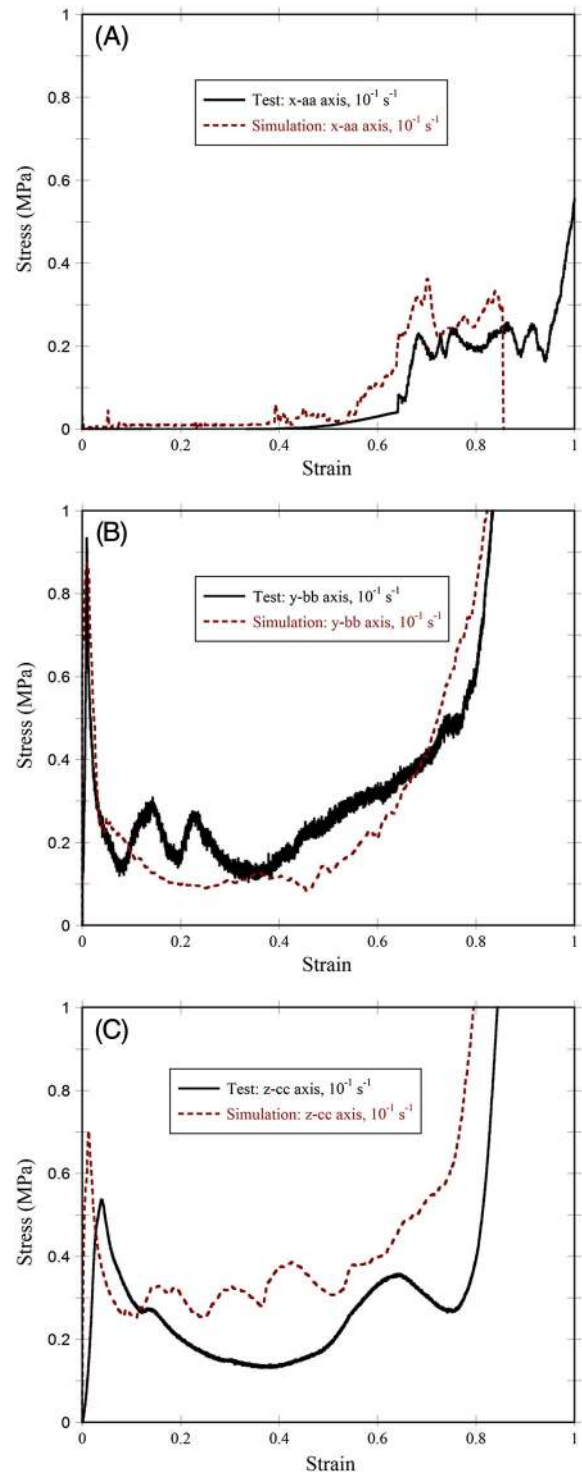

Figure 8: The experimental and simulation compression strain–stress curves of the single core layer at 10^{-1} s^{-1} in (A) *x*-aa, (B) *y*-bb and (C) *z*-cc axis

and 0.54 MPa, respectively (Figure 8B and C). Although, simulation and experimental stress–strain curves in the *y*- and *z*-axis differ from each other in stress values, the trends of the simulation and experimental stress–strain curves are
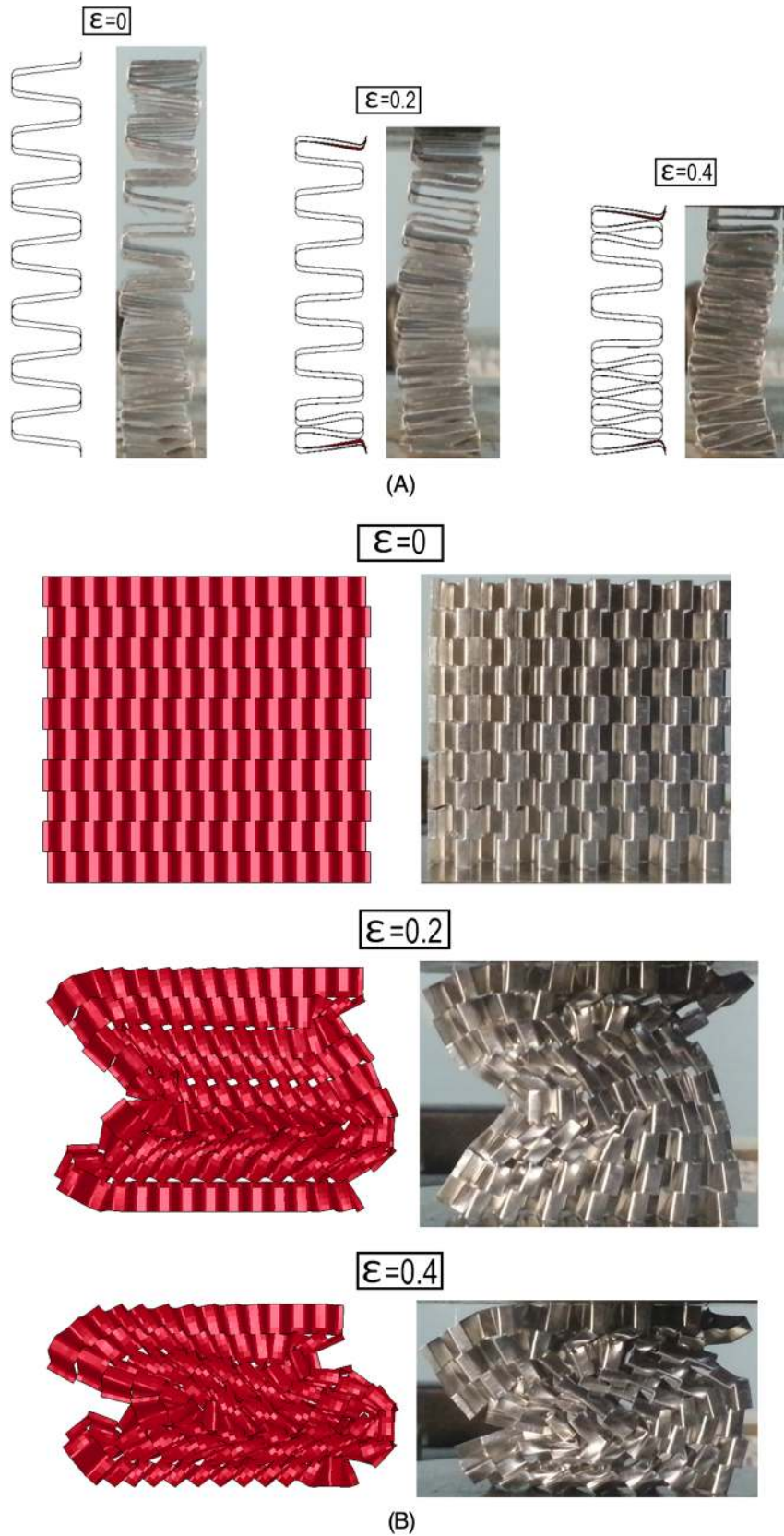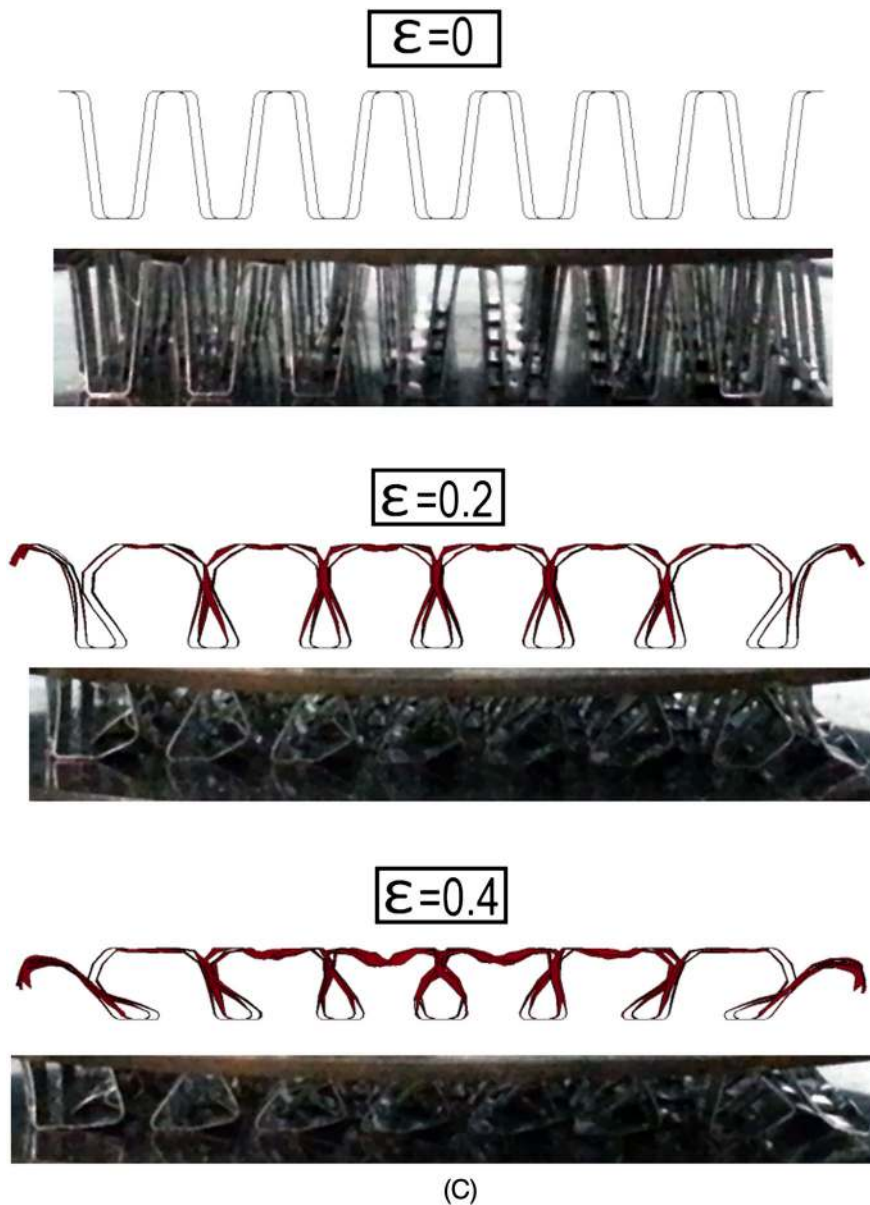
(A)

(B)

Figure 9: The simulation undeformed and simulation and experimental deformed pictures of the single core layer tested at $10^{-1}\,\mathrm{s}^{-1}$ in the (A) *x*-aa, (B) *y*-bb and (C) *z*-cc axis

$\varepsilon = 0$

$\varepsilon = 0.2$

$\varepsilon = 0.4$

(C)

Figure 9: (Continued)

nearly the same as seen in Figure 8B and C. The differences between the simulation and experimental stresses may arise from several factors. The imperfections on the fin walls tend to decrease the experimental crushing stresses. The imperfection sensitivity (bending type imperfection) was previously detected in a diamond lattice core at the quasi-static strain rates [7]. The misalignment of test specimen during testing expectedly affects the experimental stresses. Nevertheless, the effect of the above artefacts of the single core layer are included in the simulation of the multi-layer sandwich test specimens by developing MAT-26 material model based on the single fin layer experimental stress–strain curves. The elastic moduli in the *y*- and *z*-axis are measured as 133.8 and 34.35 MPa, respectively, showing highly anisotropic behaviour of the tested single core layer.

Figure 10A shows the experimental high strain rate SHPB compression front stress- $\frac{v_o t}{H}$ and quasi-static stress–strain curves of the single-layer sandwich together with those of the full and homogenized coarse mesh numerical models. The simulation initial peak stresses of the homogenized coarse mesh model (1.35 MPa) is the same with that of experiment, while the full model results in slightly lower peak stress (1.16 MPa) as seen in Figure 10A. It is noted that the full model results in similar crushing stresses with the experiment, while the homogenized coarse mesh model gives higher crushing stresses than the experiment in the
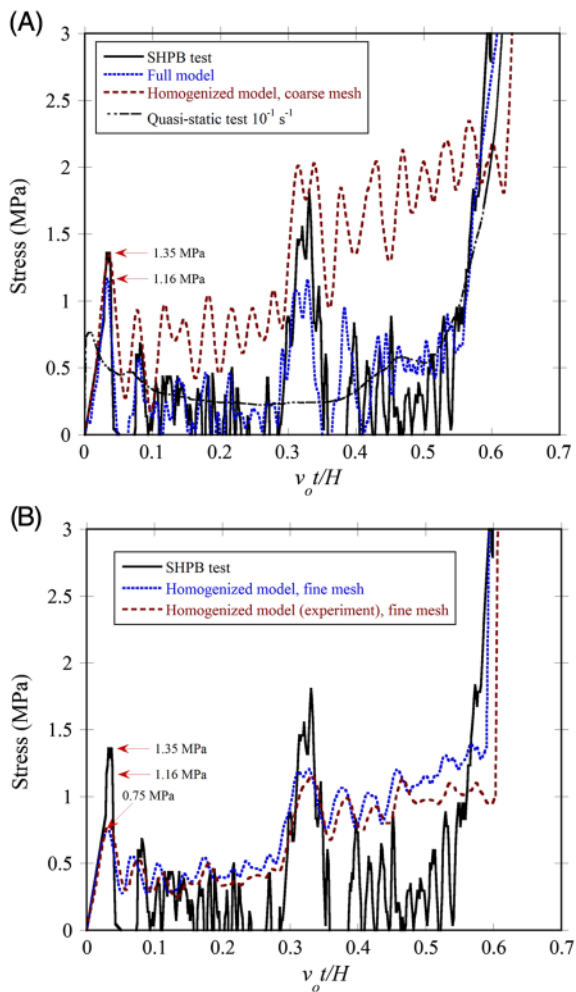
Figure 10: The experimental and simulation stress–strain curves of single-layer sandwich specimen tested in SHPB with the striker bar velocity of $18\,\mathrm{m\,s^{-1}}$; (A) test and full and coarse mesh homogenized models with quasi-static stress–strain curve and (B) test and fine mesh homogenized model and fine mesh homogenized model based on the experimental stress–strain curves of the single core layer

post-peak stress region until about the densification strain. The increased peak stress of the single-layer sandwich in SHPB test as compared with the quasi-static strain rate test shown in Figure 10A is due to the inertial effects (type II structure), which were also previously reported for the similar cellular structures including honeycombs through out of plane [20], metallic columns [21], aluminium foams [20, 22] and balsa wood in the axial direction [23]. The fine mesh homogenized model and fine mesh homogenized model based on the experimental stress–strain curve of the single core layer result in lower crushing stresses as compared with the homogenized coarse mesh model and yield comparable crushing stresses with the experiments in the post-peak stress region as shown in Figure 10B. They decrease the initial peak stress of the single-layer sandwich to the level of the quasi-static initial peak stress value,

0.75 MPa. These results show that the element size has a significant effect on the initial peak and post-peak stress values of the homogenized models. In the fine mesh homogenized models, the absence of inertial effects is reflected as the reduced initial peak stresses. The reduced initial peak stress was also reported previously in the macro modelling of a hexagonal honeycomb structure [15].

The constraint experimental and numerical compression stress–strain curves of the multi-layer specimens tested in drop weight tower are shown in Figure 11. As seen in Figure 11, the peak stresses and the post-peak stresses of the full model and the fine mesh homogenized model based on the experimental stress–strain curves of the single core layer show close agreements with the experiments, while the crushing stresses of the fine mesh homogenized model are higher than those of the experiment. Both experimental and numerical models densification strains (~0.68) closely match to each other, except the fine mesh homogenized model based on experimental stress–strain curves of the single core layer gives slightly higher densification strains (~0.7). The experimental and numerical deformed pictures of the compression tested multi-layer sandwiches are shown Figure 12A–D, respectively. The tested specimen shown in Figure 12A is compressed into the densification region, while the numerically deformed specimens shown in Figure 12B–D are compressed until about 0.4 strains in the plateau region of the stress–strain curves. In the full model shown in Figure 12B, the fin walls of all corrugated layers are seen to be elastically bent, but only the fin walls of the first top three layers are plastically collapsed via fin wall buckling. The plastic collapse is progressive, starting from the striker contact region. In the fine mesh homogenized model and fine mesh homogenized model based on the experimental stress–strain curves of the single core layer although the collapse starts from the first top layer, it
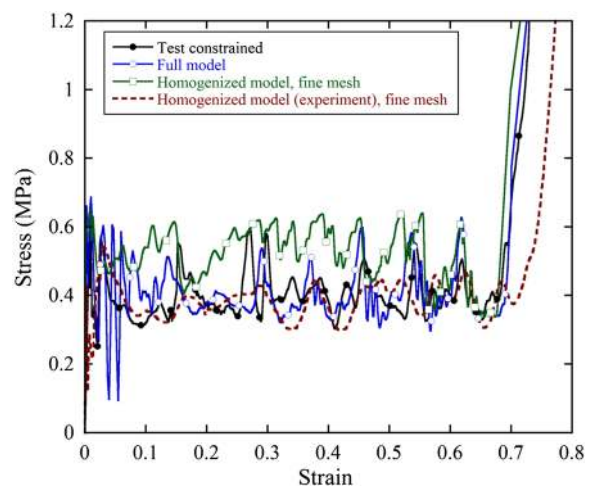

Figure 11: The experimental and simulation low velocity compression stress–strain curves of the multi-layer sandwich specimen
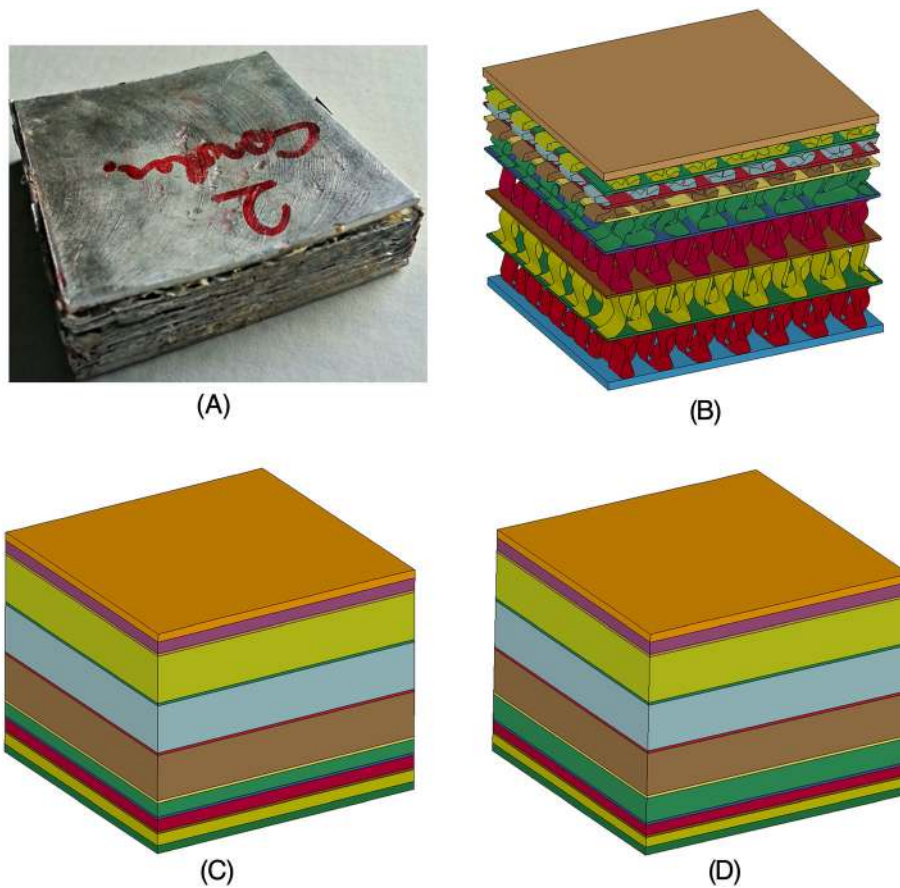
Figure 12: The deformation pictures of the low velocity compression tested multi-layer sandwich; (A) experiment, (B) full model, (C) fine mesh homogenized model and (D) fine mesh homogenized model based on the experimental stress–strain curve of the single core layer

switches to the bottom layers as seen in Figure 12C and D. The deformation trends of the full and homogenized models are however very much similar, progression with the sequential collapse of the individual fin layers.

Figure 13 shows the experimental and simulation force–displacement curves of the multi-layer sandwich specimens subjected to the low velocity indentation test. The initial linear region of the individual curves is resulted from the elastic deformation of the layers, while the plateau region from the buckling of the fin walls and bending of the face and interlayer sheets. As similar with the low velocity compression test simulations, the full model and fine mesh homogenized model based on the experimental stress–strain curves of the single core layer result in crushing loads comparable with the experiment. Figure 14A–D shows the final deformed shapes of the tested and modelled multi-layer sandwiches. The full model sandwich specimen deformation in Figure 14A is very similar with the experimental test specimen deformation in Figure 14B in that the deformation is localized along the striker–specimen contact region. The localized deformation is very anisotropic and proceeds also with the progressive fin wall buckling and interlayer and face sheet bending, starting from the
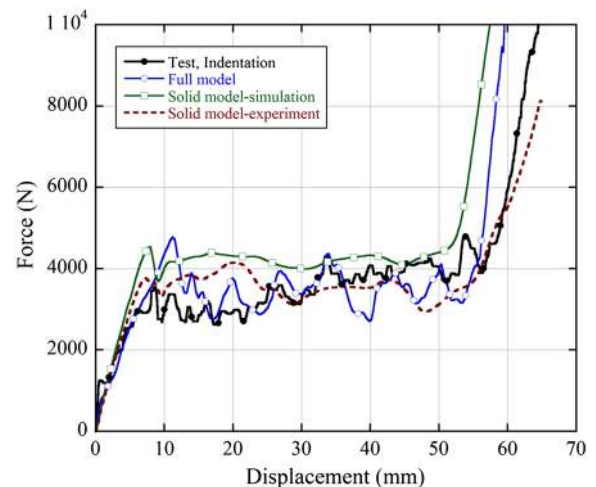

Figure 13: The experimental and simulation low velocity indentation force–displacement curves of the multi-layer sandwich specimen

striker–specimen contact region. Although the localized deformation is clearly seen at the striker–specimen contact region, the left and right edges of the homogenized model test specimens experience larger displacement compared to
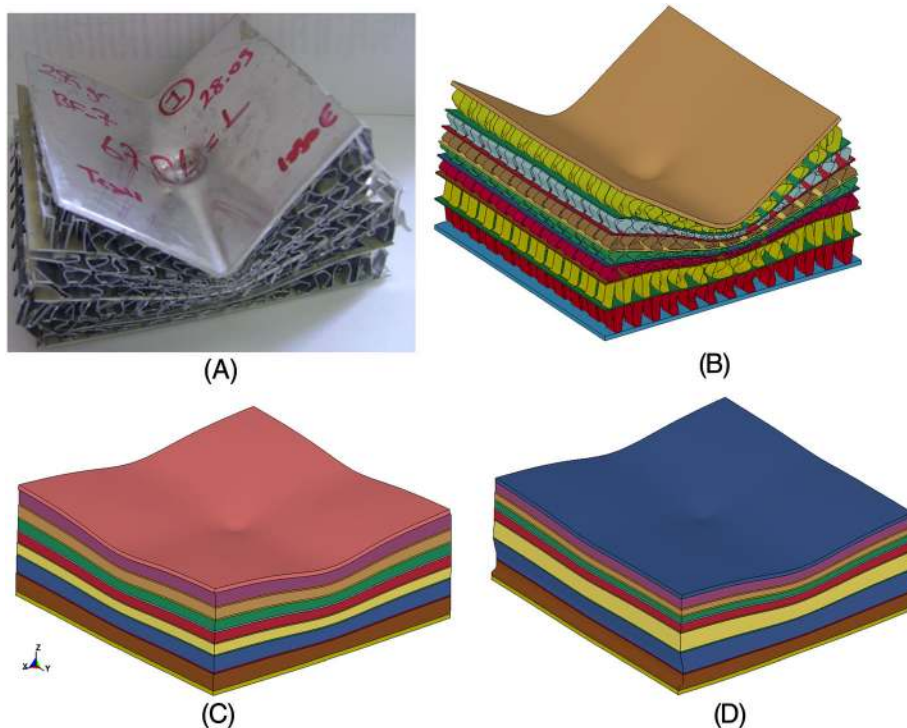
Figure 14: The deformation pictures of the low velocity indentation tested multi-layer sandwiches (A) experiment, (B) full model, (C) fine mesh homogenized model and (D) fine mesh homogenized model based on the experimental stress–strain curves of the single core layer

the full model and experimental test specimen (Figure 14A–D). This is attributed again to the lack of the inertial effects in the homogenized models.

Figure 15 shows the projectile velocity–time curves of the full and homogenized models. The experimental residual projectile velocity ($75 \, \mathrm{m \, s^{-1}}$) is also marked in the same figure for comparison. The full model results in the same residual velocity as the experiment, $75 \, \mathrm{m \, s^{-1}}$, while the
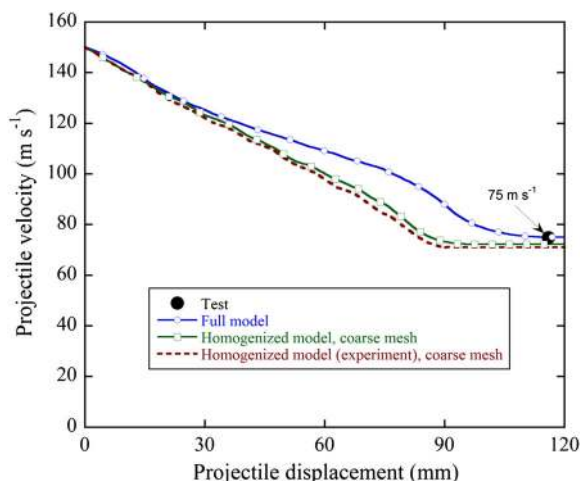

Figure 15: Numerical projectile velocity versus projectile displacement curves of the full and homogenized models of the multi-layer sandwich specimen and the experimental projectile residual velocity

coarse mesh homogenized model and the coarse mesh homogenized model based on the experimental stress–strain curves of the single core layer predict slightly lower residual velocities, 72.5 and $71 \, \mathrm{m \, s^{-1}}$, than the experiments. Until about $30 \, \mathrm{mm}$ projectile displacement, the velocity–displacement curves of the full and homogenized models are very similar; thereafter, the full model and homogenized model projectile velocities deviate from each other. The cross sections of the experimental and full model projectile impact testes specimens show also close resemblances as shown in Figure 16A and B. The face and interlayer sheets are seen to bend near the projectile perforated area in both experimental and full model test specimens. The projectile first intends the specimen; thereafter, penetration starts. The deviation between the velocity–displacement curves of the full and homogenized models is therefore presumed to start after about the projectile begins to penetrate the specimen. The higher resistances against the projectile are seen in the homogenized models than in the full model as the projectile velocity is lower in the homogenized models. The higher resistance of the solid model arises from the higher post-peak stresses of the homogenized models as shown in Figure 10A. The difference between the residual velocities of the full and homogenized models is about 5%, which lies within the experimental error range.

The homogenized models based on the experimental stress–strain curve of the single core layer predicted the low velocity compression and indentation and projectile
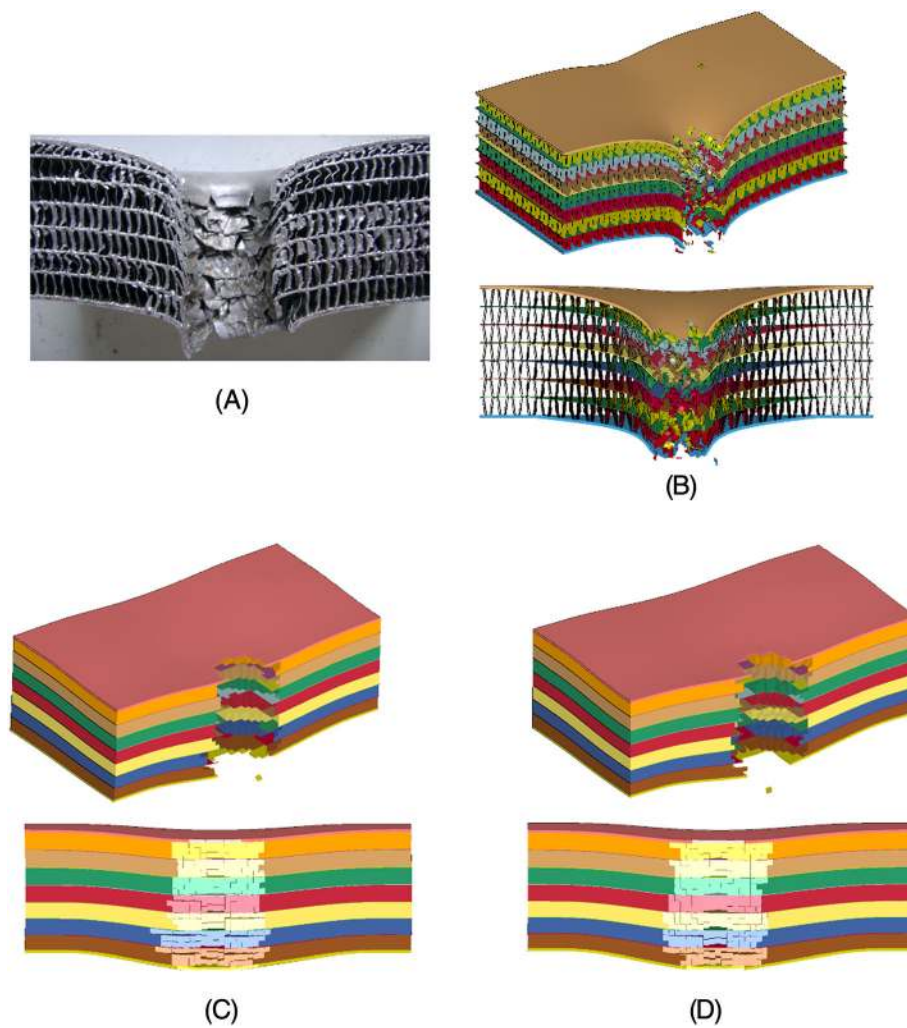
Figure 16: The cross section pictures of the projectile impact tested multi-layer sandwiches (A) experiment, (B) full model, (C) coarse mesh homogenized model and (D) coarse mesh homogenized model based on the experimental stress–strain curves of the single core layer

impact tests of the multi-layer corrugated sandwich with an acceptable accuracy and reduced the computational time of the models significantly. For the structural applications, the corrugated structure should certainly be optimized in terms of the height, width and thickness of the fins as similar with honeycomb structures [24].

Conclusions

The full and homogenized numerical models of a single core layer 1050-H14 Al trapezoidal zig-zag multi-layer corrugated sandwiches were developed base on the experimental and numerical compression tests on the single core layer. In the homogenized models, the deformation of the single fin layer was modelled using MAT-26 honeycomb model in LS-DYNA. The differences between the simulation and experimental quasi-static compression stresses of the single fin layer were attributed to the fin wall imperfections and specimen misalignment in the test. The fidelity of the full and homogenized numerical models of multi-layer corrugated sandwiches was checked via direct impact, low velocity compression and indentation and projectile impact tests. In direct impact tests, the full model resulted in similar stresses with the experiment, while the fine mesh homogenized models yielded lower initial peak stresses than the experiments due to lack of inertial effects in the homogenized models. Low velocity compression of the stress–strain curves of the full model and the fine mesh homogenized model based on the experimental stress–strain curves of the single core layer showed close agreements with each other and with those of the experiments. As similar with compression tests, the simulation of the indentation tests yielded similar force–displacement curves with the experiments. The homogenized models however exhibited higher impact resistances than the full model, which was attributed to higher post-peak stresses of the homogenized models. However, the difference between the projectile residual velocities of the full and homogenized models was found very similar, deviating 5%.

References

1. Wadley, H. N. (2006) Multifunctional periodic cellular metals. *Philos. Transact. A Math. Phys. Eng. Sci.* **364**, 31–68.

2. Sypeck, D. J., Wadley, H. N. G. (2002) Cellular metal truss core sandwich structures. *Adv. Eng. Mater.* **4**, 759–764.

3. Radford, D. D., Fleck, N. A., Deshpande, V. S. (2006) The response of clamped sandwich beams subjected to shock loading. *Int. J. Impact. Eng.* **32**, 968–987.

4. Tilbrook, M. T., Radford, D. D., Deshpande, V. S., Fleck, N. A. (2007) Dynamic crushing of sandwich panels with prismatic lattice cores. *Int. J. Solids Struct.* **44**, 6101–6123.

5. Rubino, V., Deshpande, V. S., Fleck, N. A. (2009) The dynamic response of clamped rectangular Y-frame and corrugated core sandwich plates. *Eur. J. Mech. A-solid* **28**, 14–24.

6. Hou, S. J., Zhao, S. Y., Ren, L. L., Han, X., Li, Q. (2013) Crashworthiness optimization of corrugated sandwich panels. *Mater. Des.* **51**, 1071–1084.

7. Côté, F., Deshpande, V. S., Fleck, N. A., Evans, A. G. (2006) The compressive and shear responses of corrugated and diamond lattice materials. *Int. J. Solids Struct.* **43**, 6220–6242.

8. Kılıçaslan, C., Güden, M., Odacı, İ. K., Taşdemirci, A. (2013) The impact responses and the finite element modeling of layered trapezoidal corrugated aluminum core and aluminum sheet interlayer sandwich structures. *Mater. Des.* **46**, 121–133.

9. Feraboli P., Deleo F., Wade B., Rassaian M., Higgins M., Byar A., Reggiani M., Bonfatti A., DeOto L., Masini A. (2010) Predictive modeling of an energy-absorbing sandwich structural concept using the building block approach. *Compos. Part A* **41**, 774–786.

10. Bi, J., Fang, H., Wang, Q., Ren, X. (2010) Modeling and optimization of foam-filled thin-walled columns for crashworthiness designs. *Finite Elem. Anal. Des.* **46**, 698–709.

11. Yang, S., Qi, C. (2013) Multiobjective optimization for empty and foam-filled square columns under oblique impact loading. *Int. J. Impact Eng.* **54**, 177–191.

12. Toksoy, A. K., Güden, M. (2010) Partial Al foam filling of commercial 1050H14 Al crash boxes: the effect of box column thickness and foam relative density on energy absorption. *Thin Wall Struct.* **48**, 482–494.

13. Toksoy, A. K., Güden, M. (2011) The optimisation of the energy absorption of partially Al foam-filled commercial 1050H14 and 6061T4 Al crash boxes. *Int. J. Crashworthines* **16**, 97–109.

14. Hosseini, S. M. H., Gabbert, U. (2013) Numerical simulation of the Lamb wave propagation in honeycomb sandwich panels: a parametric study. *Compos. Struct.* **97**, 189–201.

15. Lamb, A. J., Pickett, A. K., Chaudoye, F. (2011) Experimental characterisation and numerical modelling of hexagonal honeycomb cellular solids under multi-axial loading. *Strain* **47**, 2–20.

16. Odacı, İ. K., Kılıçaslan, C., Taşdemirci, A., Güden, M. (2012) Projectile impact testing of glass fiber-reinforced composite and layered corrugated aluminium and aluminium foam core sandwich panels: a comparative study. *Int. J. Crashworthines* **17**, 508–518.

17. LSTC (2007) LS-DYNA Keyword User's Manual Livermore Software Technology Corporation (LSTC).

18. Jackson, K. E. (2010) Predicting the dynamic crushing response of a composite honeycomb energy absorber using solid-element-based models in LS-DYNA. Proc. 11th International LS-DYNA® Users Conference, Detroit.

19. Calladine C. R., English, R. W. (1984) Strain-rate and inertia effects in the collapse of two types of energy-absorbing structure. *Int. J. Mech. Sci.* **26**, 689–701.

20. Zhao, H., Elnasri, I., Abdennadher, S. (2005) An experimental study on the behaviour under impact loading of metallic cellular materials. *Int. J. Mech. Sci.* **47**, 757–774.

21. Langseth, M., Hopperstad, O. S. (1996) Static and dynamic axial crushing of square thin-walled aluminium extrusions. *Int. J. Impact Eng.* **18**, 949–968.

22. Paul, A., Ramamurty, U. (2000) Strain rate sensitivity of a closed-cell aluminum foam. *Mater. Sci. Eng. A* **281**, 1–7.

23. Reid, S. R., Peng, C. (1997) Dynamic uniaxial crushing of wood. *Int. J. Impact Eng.* **19**, 531–570.

24. Hou, S. J., Ren, L. L., Dong, D., Han, X. (2012) Crashworthiness optimization design of honeycomb sandwich panel based on factor screening. *J. Sandw Struct Mater* **14**, 655–678.